Nano Research
2022, 15(3): 1699–1708

ISSN 1998-0124 CN 11-5974/O4
https://doi.org/10.1007/s12274-021-3818-9

Research Article

Near-infrared carbon nanodots for effective identification and inactivation of Gram-positive bacteria

Wen-Bo Zhao[1,§], Rui-Ting Wang[2,§], Kai-Kai Liu[1] (✉), Meng-Ru Du[3], Yong Wang[1], Yu-Qi Wang[3], Rui Zhou[1], Ya-Chuan Liang[1], Ruo-Nan Ma[3], Lai-Zhi Sui[4], Qing Lou[1], Lin Hou[2] (✉), and Chong-Xin Shan[1] (✉)

[1] *Henan Key Laboratory of Diamond Optoelectronic Materials and Devices, Key Laboratory of Materials Physics, Ministry of Education, and School of Physics and Microelectronics, Zhengzhou University, Zhengzhou 450052, China*
[2] *School of Pharmaceutical Sciences, Key Laboratory of Targeting Therapy and Diagnosis for Critical Diseases, Collaborative Innovation Center of New Drug Research and Safety Evaluation, Zhengzhou University, Zhengzhou 450001, China*
[3] *Henan Key Laboratory of Ion-beam Bioengineering, School of Agricultural Science, Zhengzhou University, Zhengzhou 450052, China*
[4] *State Key Laboratory of Molecular Reaction Dynamics, Dalian Institute of Chemical Physics, Chinese Academy of Sciences, Dalian 116023, China*
[§] *Wen-Bo Zhao and Rui-Ting Wang contributed equally to this work.*

Received: 1 July 2021 / **Revised:** 5 August 2021 / **Accepted:** 12 August 2021

ABSTRACT

An unacceptable increase in antibacterial resistance has arisen due to the abuse of multiple classes of broad-spectrum antibiotics. Therefore, it is significant to develop new antibacterial agents, especially those that can accurately identify and kill specific bacteria. Herein, we demonstrate a kind of perilla-derived carbon nanodots (CNDs), integrating intrinsic advantages of luminescence and photodynamic, providing the opportunity to accurately identify and kill specific bacteria. The CNDs have an exotic-doped and π-conjugated core, vitalizing them near-infrared (NIR) absorption and emission properties with photoluminescence quantum yield of 21.1%; hydrophobic chains onto the surface of the CNDs make them to selectively stain Gram-positive bacteria by insertion into their membranes. Due to the strong absorption in NIR region, reactive oxygen species are *in situ* generated by the CNDs onto bacterial membranes under 660 nm irradiation, and 99.99% inactivation efficiency against Gram-positive bacteria within 5 min can be achieved. *In vivo* results demonstrate that the CNDs with photodynamic antibacterial property can eliminate the inflammation of the area affected by methicillin-resistant *Staphylococcus aureus* (MRSA), and enabling the wound to be cured quickly.

KEYWORDS

carbon nanodots, near-infrared emission, specific identification, anti-bacteria, photodynamic therapy

1 Introduction

Antimicrobial resistance of bacteria and the associated mortality caused by bacterial pathogens are increasing to alarming levels. It is estimated that by 2050, 10 million lives a year may be lost to bacteria with antimicrobial resistance, exceeding death toll (8.2 million) caused by cancer [1]. The increases use of global antibiotics and inappropriate use of antibiotics in medical practice are one of the prime reasons [2]. Another important reason is that broad-spectrum antimicrobials can kill most bacteria, leading to an increased chance of bacteria emerging with drug-resistant genes [3–5]. As a result, some pathogens evolve resistance, and a suite of side-effects on host and pathogen would emerge. In comparison, narrow-spectrum antibiotics do not generate cross-resistance in non-targeted pathogens, thus development of narrow-spectrum antibiotics as an attractive approach can overcome multidrug-resistant bacterial infections. In general, specific bacteria-killing agents need to have the following characteristics: Firstly, the agents should have a specific response, which can distinguish the Gram-positive bacteria and Gram-negative bacteria; secondly, the agents must have excellent antibacterial properties in order to kill pathogenic bacteria; finally, the agents must ensure sufficient safety while killing the specific bacteria, and will not lead to antimicrobial resistance of the bacteria. Therefore, rapid and reliable discrimination and inactivation of bacteria are crucial for anti-bacterial application.

The fluorescence labeling method based on fluorescent nanoparticles (NPs) or molecules is an effective approach for discriminating bacteria [6, 7], which has advantages of fast response, high sensitivity, high reproducibility and short procedure time compared with traditional methods such as Gram staining, plate culture [8], polymerase chain reaction [9] and immunological methods [10], etc. Thus, fluorescent nanoparticles with antibacterial agents or some cationic polymers were used to identify bacteria and kill specific strains of bacteria, through the synergy of electrostatic attraction and hydrophobic action [11, 12]. Although such methods can selectively kill bacteria, they still have some drawbacks such as complex synthesis, detachment of the cationic polymers from NPs surface and compromised antibacterial efficacy [13, 14]. In addition, most positively charged substances have been found to be highly toxic to mammalian cells [15]. Furthermore, usage of linked antimicrobial agents may also

Address correspondence to Kai-Kai Liu, liukaikai@zzu.edu.cn; Lin Hou, houlin@zzu.edu.cn; Chong-Xin Shan, cxshan@zzu.edu.cn

increase bacterial resistance, and thus causing injure of specific cells. Antimicrobial photodynamic therapy is being actively investigated as possible alternative to antibiotic treatment for wound infections [16–20]. Reactive oxygen species (ROS) produced under light irradiation can destroy many components of cells. In particular, photodynamic antibacterial under illumination of near-infrared (NIR) light (biological window), can effectively kill bacteria in infected tissues without creating bacterial resistance [21–26]. Therefore, it is essential to design safe and potent photodynamic sterilization agents activated by NIR light that can accurately identify and kill specific bacteria.

Carbon nanodots (CNDs), an emerging member of fluorescent nanomaterials [27, 28], are currently playing an important role in the antimicrobial field due to their abundant source of precursors, rich surface groups, and excellent photoelectron conversion properties [29–31]. It has been demonstrated that CNDs can be used as potent antibacterial agents [32, 33]. Li et al. synthesized CNDs by an electrochemical method with vitamin C as precursor, and investigated their broad-spectrum antibacterial activities against *S. aureus*, *B. subtilis*, *Bacillus sp*, *E. coli*, and the ampicillin-resistant *E. coli* [34]. Wu et al. prepared quaternary ammonium salt modified CNDs using a carboxyl-amine reaction against Gram-positive bacteria [35]. However, CNDs with NIR absorption/emission for simultaneous discrimination and inactivation of bacteria without any complicated modifications have rarely been reported.

Herein, hydrophobic CNDs with near-infrared absorption and emission using low-cost, non-toxic perilla as a precursor have been prepared. The hydrophobic groups onto the surface of the CNDs can be easily inserted into the cell membrane of Gram-positive bacteria by hydrophobic interaction rather than electrostatic interaction, as illustrated in Fig. 1. When the CNDs were incubated with bacteria, they were close to the Gram-positive bacteria, while distant from Gram-negative bacteria in a mixture. In addition, the strong NIR absorption of CNDs enables them to possess excellent photoelectron conversion capabilities and can generate ROS under excitation of 660 nm light. Thus, ROS are *in situ* generated on the surface of Gram-positive bacteria membranes when the CNDs are inserted into bacteria, causing damage to the cell membranes and inactivation of Gram-positive bacteria. It is noting that the CNDs can kill methicillin-resistant staphylococcus aureus (*MRSA*) with a sterilizing rate of 99.99% under irradiation of 660 nm light for 5 min. The healing of wounds infected by *MRSA* is faster under the treatment of the CNDs compared with that of the wounds without treatment.

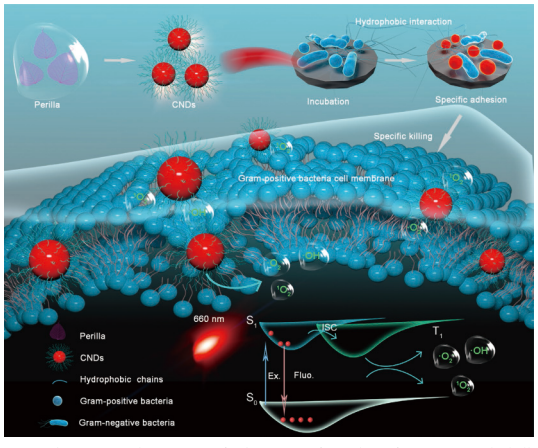

Figure 1 Schematic diagram of the specific identification and killing of bacteria by the CNDs and the corresponding antibacterial mechanism.

2 Experimental section

2.1 Materials and characterization

Perilla leaves were purchased from local markets. They were washed and dried before use. Ethanol (> 99.7%, purity) was purchased from Shanghai Maclean Biochemical Technology Co., Limited. The fluorescent dyes reflecting the relevant indicators of bacterial membranes were as follows: LIVE/DEAD BacLight Bacterial Viability Kit (L701, 161 Invitrogen, USA) and a fluorescent probe of 2',7'-dichlorofluorescein 186 diacetates for intracellular ROS level (DCFH-DA) (S0033, Beyotime, China). The membrane potential of bacteria was analyzed by 3,3-diethyloxacarbocyanine iodide (DiOC2(3)) (B34950, Invitrogen). The transmission electron microscopy (TEM) and high-resolution TEM (HRTEM) images of the CNDs were characterized by a Tecnai G20 TEM. Atomic force microscopy (AFM) images were recorded by a Multimode 8 instrument. The Fourier transform infrared (FTIR) spectra of the samples were recorded using a Thermo Scientific Nicolet IS10 FTIR spectrometer. The X-ray photoelectron spectroscopy (XPS) spectra of the samples were collected by using a Thermo Fisher Scientific ESCALAB 250Xi spectrometer. The photoluminescence (PL) and ultraviolet–visible (UV–vis) spectra were recorded by a Hitachi F-7000 and UH4150 spectrophotometer, respectively. The lifetimes of the CNDs were measured on a FLS920 spectrometer with excitation of 405 nm. The electron paramagnetic resonance (ESR) spectra of the CNDs were recorded by an electron paramagnetic resonance spectrometer (Bruker A300). The bacterial imaging pictures were taken at a Leica TCS SP8 laser scanning confocal microscope. The membrane potential of bacteria was quantified using a flow cytometer (NovoCyte 2060, ACEA).

2.2 Preparation of CNDs

A typical preparation of CNDs by using a hydrothermal method was as follows: First, perilla leaves (2 g) and 20 mL of ethyl alcohol were transferred to a poly (tetrafluoroethylene) (Teflon)-lined autoclave (50 mL) and heated at 140 °C for 2 h. After the reaction was completed, the reactor was automatically cooled to room temperature. The reaction solution was then taken, filtered through a 0.22 μm nylon membrane and dried at 60 °C for 6 h to obtain the sample powder.

2.3 Water-octanol partition coefficient (log *P*)

The CNDs were added into n-caprylic alcohol solution, with volume ratio of 1:1. The above solutions were mixed well and left to equilibrate in the dark for 24 h. Subsequently, the solutions in the different dispersed phases were diluted 10 times with methanol and the respective UV–vis spectra were recorded. The concentration of the CNDs in each disperse phase was calculated by a standard curve. The partition coefficient was defined as

$$\log P = \log (C_1/C_2) \quad (1)$$

where C_1 and C_2 are the CNDs concentrations in n-caprylic alcohol and water, respectively.

2.4 Bacterial culture

To illustrate the bacterial culture process, we took *S. aureus* as an example, as follows: A single colony of *S. aureus* was inoculated in 20 mL of Luria-Bertani (LB) medium (pH = 7) at 37 °C, 180 rpm for13h.1mLoftheaboveliquidwasaddedtoafresh20mLLBmediumat 37 °C, 210 rpm and shaken for 2 h to a concentration of 10^9 cfu/mL. Other types of bacteria were cultured in the same way.

2.5 Bacterial imaging assay

1 mL bacterial solution at a concentration of 10^9 cfu/mL was transferred to 2 mL eppendorf (EP) tube. Bacteria were harvested by centrifugation at 5,000 rpm for 5 min, followed by removal of the supernatant. 1 mL of CNDs solution (dimethyl sulfoxide (DMSO)/water) at a certain concentration was then added into the EP tube and mixed uniformly. The EP tubes were placed in dark conditions and incubated for 30 min. Then the CNDs/bacterial mixture was centrifuged at 5,000 rpm for 5 min and the supernatant poured off. Washing was continued by adding 1 mL of phosphate buffered saline (PBS) and centrifuging again, this process was repeated 2 times. Finally, the bacterial precipitate was placed on a glass slide and observed using a confocal microscope (TCS SP8, Leica, Germany) under the condition: excitation: 405 nm, emission range: 600–750 nm.

2.6 Antibacterial activity measurement of CNDs

100 μL of bacteria at a concentration of 10^9 cfu/mL was added to 900 μL of different concentrations of CNDs aqueous solution to obtain a CNDs/bacteria mixture with a bacterial concentration of 10^8 cfu/mL. The solution was sequentially irradiated with a 660 nm lamp (200 mW/cm^2) for 5 min and the control group was placed in the dark for 5 min. The viability of bacteria was quantified by a plate-count method. The bacteria were diluted with a dilution factor of 10^6,10^5,10^4,10^3 and 10^2. Then 100 μL of the bacteria solution was evenly spread on an LB agar plate, which was then subjected to culturing at 37 °C for 20 h before quantification and photo taking.

2.7 Determination of MBC_{90}

1 mg/mL of CNDs aqueous solution was prepared and then sequentially diluted with PBS to 0.01, 0.009, 0.008, 0.007, 0.006, 0.005, 0.004, 0.003, 0.002 and 0.001 mg/mL. 100 μL of bacteria was added to each of the above solutions to obtain a volume of 1 mL of bacterial/CNDs mixed with a bacterial concentration of 10^8 cfu/mL. It was then treated with 660 nm light for 5 min. The samples were diluted using sterile PBS and 100 μL of the diluted samples was spread on ager plate in triplicate. All the plates were incubated at 37 °C for 20 h. The colony-forming units were counted and analyzed.

2.8 Live/dead staining

The confocal laser scanning microscopy (CLSM) was used to visually evaluate the live/dead bacteria, which were stained with the LIVE/DEAD BacLight Bacterial Viability Kit (L701, 161 Invitrogen, USA). After treatment with CNDs, the bacterial suspension was collected and washed 3 times with PBS. The treated bacteria were placed on SYTO-9 and PI double-stained medium and incubated in a dark at 37 °C for 15 min. The stained bacteria were then washed twice with PBS and observed under three different microscopic fields using CLSM.

2.9 Intracellular ROS detection

The bacterial suspension was added to PBS containing 10 μM DCFH-DA and treated with 660 nm light for 5 min. The control group was incubated in the dark for 5 min. Then bacteria were washed twice with PBS and harvested for 5 min CNDs treatment. All samples were measured immediately by flow method flow cytometry (FCM), and at least 10,000 cells were monitored by FCM for each measurement.

2.10 Membrane potential measurement of the *S. aureus* and *E. coli*

For the positive control group, 2 μL of 500 μM carbonyl cyanide 3-chlorophenylhydrazone (CCCP) was added into the *S. aureus* and *E. coli* suspensions. For the treatment group, 1 mL of the *S. aureus* suspensions after CNDs treatment under dark and light conditions was centrifuged and re-suspended in 1 mL of PBS. 2 μL of 3 mM DiOC2(3) was added to the above *S. aureus* suspension for 30 min at room temperature and monitored by FCM. For the *E. coli* group, the procedure for membrane potential detection was carried out as described above.

2.11 Mouse infection model

To evaluate the antibacterial efficacy *in vivo*, one kind of infection mode was developed. Male BALB/c mice were purchased from Hunan SJA Laboratory Animal Co., Ltd (Hunan, China). All animal procedures were performed in Institute of Drug Discovery & Development of Zhengzhou University (syxk (yu) 2018-0004) and in accordance with the guidelines for Care and Use of Laboratory Animals of Zhengzhou University. The hind hairs of the mice were shaved, and the animals were anesthetized by intraperitoneal injection of sodium pentobarbital (40 mg/kg). A full-thickness skin wound (Approx. 10 mm × 10 mm) (n = 3) was created by excising the back skin of mice. The wounds were infected with 10 μL (10^8 cfu/mL) of *MRSA*. After 24 h, the wound was treated by the CNDs. Briefly, the wounds were treated with 50 μL of 0.20 mg/mL CNDs in PBS, with or without 660 nm light for 5 min. For the control group, wounds were treated with PBS exposed to the 660 nm light for 5 min. The mice were housed in individual cages and their weight and wound size were recorded daily. At the end of the corresponding experiments, all mice were euthanized. Subsequently, the tissue collected from the infected wound was fixed in 4% paraformaldehyde, embedded in paraffin, and cut into 4 μm sections. The samples were stained with hematoxylin-eosin (H&E) and Masson. A brightfield microscope was used to observe the sample.

2.12 *In vivo* safety test

Mice were treated with 200 μL CNDs (0.20 mg/mL) for 1 day and 7 days via intravenous injection. Then mice were sacrificed and harvested heart, kidney, bladder, liver, and lung. The principle organs were excised and immediately fixed in neutral fixative for histopathological examination.

3 Results and discussion

3.1 Characterization of the CNDs

Transmission electron microscope (TEM) image of the CNDs was taken, as shown in Fig. 2(a). The CNDs with a diameter of about 2.5 nm can be observed, and the corresponding size distribution is shown in Fig. S1 in the Electronic Supplementary Material (ESM). From the high-resolution TEM images of the CNDs (inset of Fig. 2(a)), the well-resolved lattice fringes with an interplanar spacing of 0.24 nm of the CNDs can be observed, corresponding to the (1120) facet of graphene [36, 37]. The height distribution of the CNDs ranges from 6 to 10 nm can be observed from the AFM image, as shown in Fig. 2(b). The CNDs are prone to aggregation in silicon substrate (for AFM) compared with copper grid substrate (for TEM), which leads to the larger sizes observed in AFM. FTIR spectroscope was used to analyze the surface states and functional groups of the CNDs. In Fig. 2(c), the absorbance peak at 3,300 cm^{-1} is attributed to the stretching vibrations of O–H. The peaks at 2,920 and 2,850 cm^{-1} are attributed to the $-CH_3$ and $-CH_2$ symmetric stretching, respectively [38], which indicates that the surface of the CNDs contains a series of hydrocarbon groups [35]. Stretching vibrations of C=O, C–C, and C–O–C are localized at about 1,630, 1,460, and 1,150 cm^{-1},

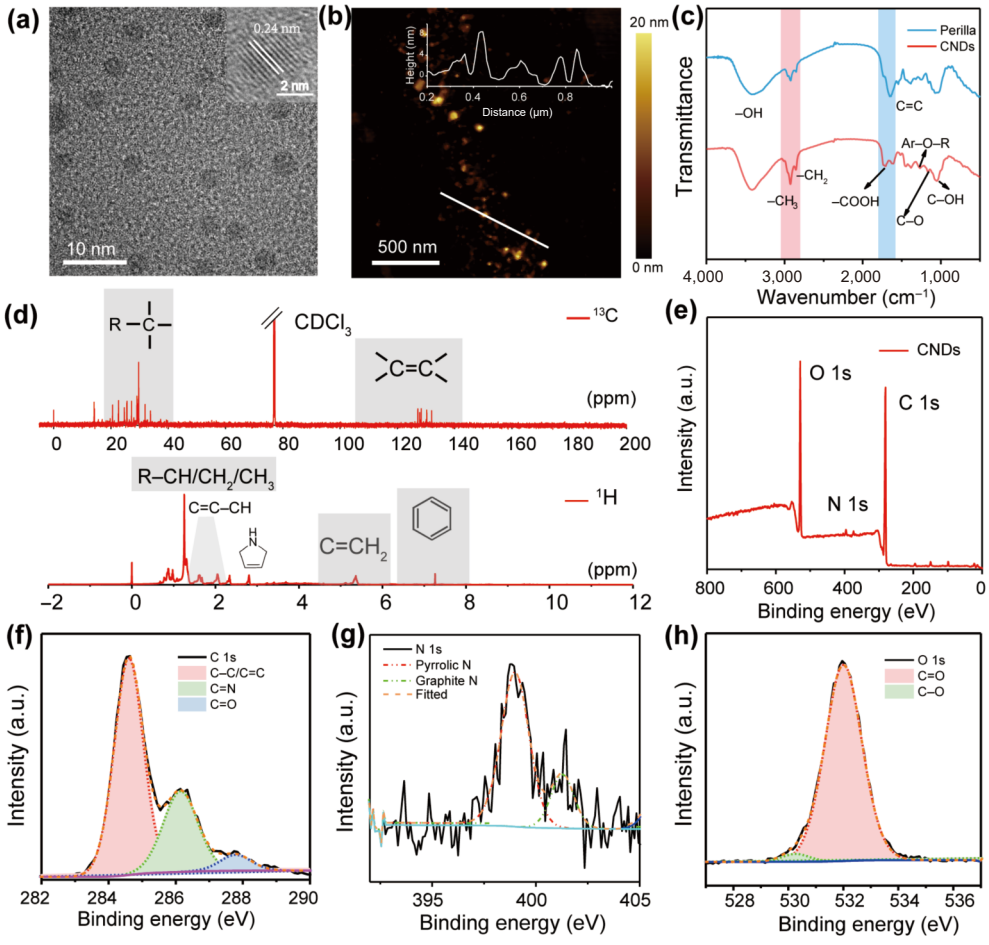

Figure 2 (a) TEM and corresponding HRTEM image (inset) of the CNDs. (b) AFM image of the CNDs. (c) FTIR spectra of the perilla and CNDs. (d) ^{13}C and ^{1}H NMR spectra of the CNDs. (e) XPS survey spectrum of CNDs, and high-resolution (f) C 1s, (g) N 1s, and (h) O 1s XPS spectra of the CNDs, respectively.

respectively [39, 40]. The FTIR spectrum of the CNDs reveals that they have abundant hydrocarbon chains, carboxyl and hydroxy functional groups on the surface of the CNDs. To investigate the internal structure of the CNDs, ^{1}H nuclear magnetic resonance (^{1}H NMR) and ^{13}C NMR spectra were measured, as shown in Fig. 2(d). In the ^{13}C NMR spectrum, the signals presented in the range of 110–140 ppm can be ascribed to sp^2 conjugated aromatic C atoms [41]. Obvious signals are observed in lower chemical shifts (0–40 ppm), which are assigned to sp^3 C atoms. In the ^{1}H NMR spectrum, aromatic H centered at 7.3 ppm can be observed clearly. Other H signals from –C–H/–C–CH_2/–C–CH_3 (0–2.5 ppm), pyrrole H (2.5–3.0 ppm), and C=CH_2 (5.0–6.0 ppm) are also detected [42]. Moreover, the surface state composition of the CNDs was characterized by XPS. The spectrum presented in Fig. 2(e) shows typical peak of C 1s (284.8 eV), N 1s (399.6 eV), and O 1s (532.0 eV), and the atomic ratios of these elements are 75.7%, 1.1% and 23.2%, respectively. High-resolution XPS spectra depict the detailed binding between C, N and O atoms. The high-resolution spectrum of C 1s shown in Fig. 2(f) exhibits three peaks at 284.6, 285.8, and 288.0 eV, which are assigned to the C–C/C=C, C=N and C=O bonds, respectively [38, 43]. The N 1s spectrum (Fig. 2(g)) shows two peaks at 400.1 and 401.9 eV, which can be attributed to pyrrolic N, and graphitic N, respectively [41]. These results suggest that the presence of nitrogen in the CNDs is in the form of pyrrole nitrogen and a small part of graphite nitrogen. The O 1s spectrum with two peaks centered at around 531.6 and 532.9 eV are assigned to C=O and C–O (Fig. 2(h)). The above characterizations identify that the CNDs have a π-conjugated core consisting of aromatic rings and N heterocycles and have hydrocarbon chains on the surface.

3.2 Optical properties of the CNDs

The PL spectrum of the CNDs shown in Fig. 3(a) shows that the main emission peak is centered at around 660 nm with a quantum yield of 21.1%. The UV–vis absorption spectra of the CNDs were also collected, as shown in Fig. 3(b). A wide absorption range from 400 to 750 nm can be observed, with two stronger absorption peaks located at 420 and 660 nm, respectively. The two strong absorption peaks could be attributed to n–π* transition caused by N and O atom doping [44]. Polysaccharides and proteins of perilla were carbonized under high temperature, and a conjugated inner core formed inside of the CNDs, thus endows the CNDs with excellent optical properties. Hydrophobic hydrocarbon chains that existed on the surface of the CNDs make them with hydrophobicity and a corresponding water-octanol partition coefficient (log *P*) of CNDs is 1.1 as measured by a shake flash method (Fig. S2 in the ESM). When log *P* is greater than 0, the CNDs are considered to be relatively hydrophobic [45]. Appropriate ultrasound can disperse the CNDs in water and PBS (Fig. S3 in the ESM). Meanwhile, the stability of the CNDs in biological fluids was determined. A RPMI1640 medium (containing 10% fetal bovine serum) was chosen as the dispersion solution and the corresponding dynamic light scattering test was recorded. The dynamic light scattering (DLS) result indicates that the average size of the CNDs in RPMI1640 medium (containing 10% fetal bovine serum) was 226.9 nm (Fig. S4 in the ESM), indicating the CNDs do not break down. The larger size than that of observed in TEM image is owing to the existence of hydrophobic chains on the surface of the CNDs. The fluorescence lifetime of the CNDs is longer in DMSO compared that of in aqueous solution and decreases as the water content increases

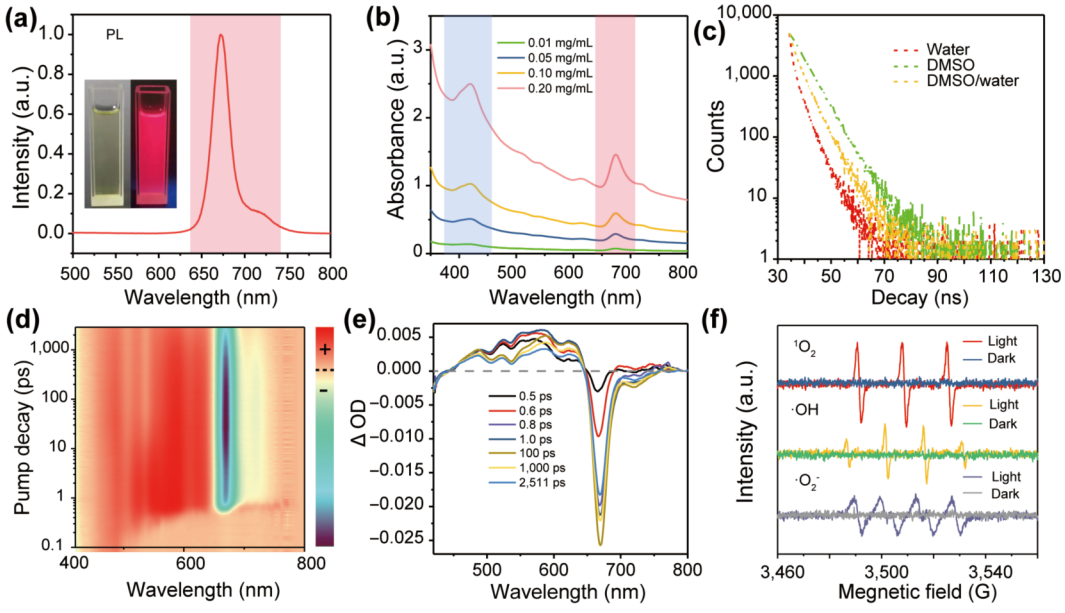

Figure 3 (a) PL spectrum of the CNDs, the inset is the image of the CNDs under sunlight and UV illumination. (b) UV–vis absorbance spectra of the CNDs with different concentrations in water. (c) Decay curves of the CNDs detected at 660 nm in different solutions. (d) 2D top-view TA spectra of the CNDs. (e) TA spectra of the CNDs at the indicated time from 0.5 to 3,000 ps under excitation of 400 nm fs-laser. (f) ESR spectra of the CNDs for detection of $^1O_2$, ·OH and $·O_2^-$ in the dark condition and under the illumination of 660 nm light, respectively.

(Fig. 3(c)), suggesting that the presence of water leads to fluorescence quenching due to aggregation of the CNDs. To further understand the PL mechanism, femtosecond transient absorption (TA) spectra were recorded, as shown in Fig. 3(d). Two-dimensional (2D) TA spectra with excitation at 400 nm, probe at 400–900 nm with delay times from 0.5 to 3,000 ps were collected. A series of clearly positive signals presented between 450 and 650 nm can be observed, corresponding to typically excited state absorption (ESA). A negative signal between 650 and 750 nm encapsulates information on ground-state bleaching (GSB) and stimulated emission (SE) [46–48]. Combined with the emission and absorption spectra of the CNDs, the signals shown in the range of 670–720 nm reveal SE property of the CNDs (Fig. 3(e)). The GSB signal located in the range of 650–670 nm is consistent with the absorption spectrum. TA kinetic traces of the CNDs probed at different wavelengths exhibit temporal evolution of GSB and SE process, as shown in Fig. S5 in the ESM. The superior optical properties and suitable hydrophobic properties enable the CNDs as an alternative fluorescence probe for the selective imaging of different bacteria species. To evaluate specific identification property of the CNDs, 6 kinds of commonly used bacteria were selected, represented by Gram-positive bacteria (*Staphylococcus aureus*, *MRSA* and *Bacillus cereus*) and Gram-negative bacteria (*Escherichia coli*, *Salmonella*, and *Pseudomonas aeruginosa*).

Surprisingly, after incubating the CNDs with all the bacteria for 30 min, we found that only the positive bacteria could be stained by the CNDs, while the negative bacteria were not stained, indicating a significant selectivity (Fig. S6 in the ESM). The apparently selective identification behavior can be explained by electrostatic and hydrophobic interactions between the CNDs and bacteria [16, 49]. To investigate the detailed interaction mechanism, zeta potentials of the CNDs and various bacteria were measured, as shown in Fig. S7 in the ESM. Both Gram-positive, Gram-negative bacteria and the CNDs are negatively charged, so electrostatic attraction was not the reason for selective identification. In addition, the log *P* vaule of the CNDs was measured to be 1.1 by the shake flask method. It is well established that hydrophobic materials have a different affinity for bacteria due to differences in the cell membrane components between Gram-positive and Gram-negative bacteria. The greater the hydrophobicity of the materials the higher affinity it has for negative bacteria, while the less hydrophobic properties make it adherent to positive bacteria [50]. Thanks to the suitable log *P* value and the exclusion of electrostatic attraction, the hydrophobic interactions are the main reason for selective identification of bacteria. Furthermore, the content of ROS, in the aqueous solution of CNDs under 660 nm conditions was measured. The contents of $^1O_2$, ·OH and $·O_2^-$ were detected by ESR using 5,5-dimethyl-1-pyrroline N-oxide (DMPO) and 2,2,6,6-tetramethylpiperidine-1-oxyl (TEMPO) as spin probes, as shown in Fig. 3(f). There is no signal generated in the sample solution under dark conditions. Obvious signals can be observed under illumination of 660 nm light, which are assigned to singlet oxygen, hydroxyl radicals, and superoxide anion, respectively [17]. Singlet oxygen sensor green (SOSG) was also used to test the ability of CNDs to produce $^1O_2$ [51]. In Fig. S8 in the ESM, there is almost no green fluorescence signal of SOSG in the system at 0 min, and the green fluorescence signal increases gradually after 5 min of 660 nm light illumination. The level of $^1O_2$ in the solution system was positively correlated with irradiation time, and the content of $^1O_2$ was always increasing over the 5 min irradiation, indicating that CNDs can produce $^1O_2$ steadily. These results clearly show that the CNDs have excellent photodynamic properties and these ROS generated by CNDs play important roles in photodynamic sterilization.

3.3 Photodynamic antibacterial activity

Inspired by the structural characteristics and bacterial discrimination ability, the photodynamic antibacterial properties of the CNDs were further evaluated in addition to specific identification. *S. aureus*, *MRSA* as representative of Gram-positive bacteria and *E. coli* as a representative of Gram-negative bacteria were used as study sterilizing effect of the CNDs under the same conditions. The initial concentration of *S. aureus* was 10^8 cfu/mL and there was no significant decrease in the number of *S. aureus* with the increase of the CNDs' concentration under dark conditions (Fig. 4(a)). While under illumination of 660 nm light for 5 min, the corresponding colony count decreased from 10^8 to 10^4 cfu/mL while the concentration of the CNDs gradually increased from 0

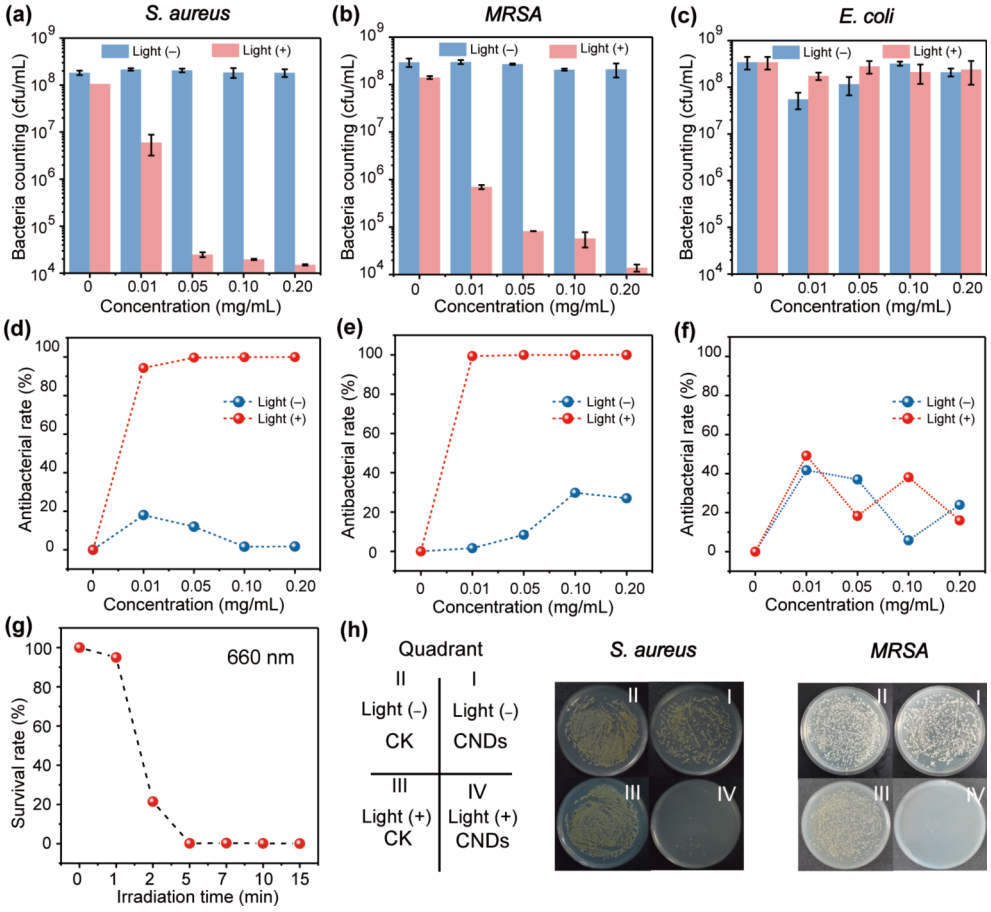

Figure 4 The number of *S. aureus* (a), *MRSA* (b) and *E. coil* (c) treated by the CNDs with different concentrations under dark and light (660 nm) conditions. (d)–(f) Inactivation rate of *S. aureus*, *MRSA* and *E. coli*. (g) Survival rate of *S. aureus* treated with the CNDs for different irradiation times. (h) Flat counting images treated with and without the CNDs under dark and light conditions.

to 0.20 mg/mL. The concentration of the CNDs is 0.20 mg/mL, the bactericidal rate can reach 99.99% (Fig. 4(d)). Besides the common *S. aureus*, the inactivation effect of the CNDs on *MRSA* was also studied. *MRSA* is one of the Gram-positive bacteria that is resistant to almost all β-lactam antibiotics and may also show resistance to a wide range of antibacterial agents such as macrolide antibiotics and aminoglycoside antibiotics, and has become one of the essential pathogens of intra-hospital and community infections [52]. While multi-drug resistant bacteria are insensitive to antibiotics, they are defenseless against ROS produced by the CNDs. The colony counts of *MRSA* after incubation with CNDs are shown in Fig. 4(b). Upon exposure to 660 nm light, the number of colony of *MRSA* drastically decrease from an initial 10^8 to 10^4 cfu/mL in a period of 5 min and inactivation efficiency of 99.99% can be achieved (Fig. 4(e)). The killing effect on *E. coli* of the CNDs was negligible, decrease the number of colony counts is no obvious decrease compared with the control group. The antibacterial result of the CNDs against *E. coli* is shown in Fig. 4(c), and the number of bacteria is both higher than 10^8 cfu/mL under light or dark conditions. The corresponding bactericidal efficiency is not more than 50% (Fig. 4(f)), demonstrating the non-toxicity of the CNDs against *E. coli*. Besides, the sterilizing rate of the CNDs against *Enterococcus faecalis* (Gram-positive bacteria) and *Salmonella* (Gram-negative bacteria) was also recorded, as shown in Figs. S9 and S10 in the ESM. The sterilizing rate of the CNDs against *Enterococcus faecalis* can reach 99.9%, while that of the CNDs against *Salmonella* is less than 50%. The results show that there was a significant difference between the Gram-positive and Gram-negative bacteria groups after treated with the CNDs under the illumination of 660 nm light, indicating that the CNDs can specifically identify and inactivate Gram-positive bacteria. Furthermore, the experiment of light irradiation time on sterilizing rate of Gram-positive bacteria was performed, and 99.99% of *S. aureus* could be inactivated within 5 min. Nearly 100% sterilizing rate can achieve after exposure to light beyond 5 min (Fig. 4(g)). Flat counting images of *S. aureus* and *MRSA* with different treatment conditions are shown in Fig. 4(h). Quadrants I, II, III, and IV refer to bacteria/CNDs without light, bacteria without light, bacteria with light, and bacteria/CNDs with light, respectively. It can be seen that the colony count almost completely disappears after treatment with the CNDs under the illumination of 660 nm light. The above data demonstrates that the CNDs can selectively and efficiently kill Gram-positive bacteria, even for multi-drug resistant bacteria. Minimum bactericidal concentration (MBC_{90}) is defined as the lowest concentration of anti-bacteria agent that kills 90% of the initial bacterial population [53]. The MBC_{90} value of CNDs against *MRSA* was measured as shown in Table S1 in the ESM, which is comparable to a commercial photosensitizer (Chlorin e6). Considering that the CNDs can be produced at a low cost of $0.09 per gram, and their antimicrobial properties are comparable to Chlorin e6 ($1,999 per gram), the CNDs are a promising antimicrobial agent.

3.4 Antibacterial mechanisms

A reasonable explanation for specific identification and inactivation of Gram-positive bacteria by the CNDs is illustrated in Fig. 5(a). Firstly, the CNDs can selectively adhere to the Gram-positive bacteria due to the presence of hydrophobic chains on the surface of CNDs, which has been confirmed by the partition

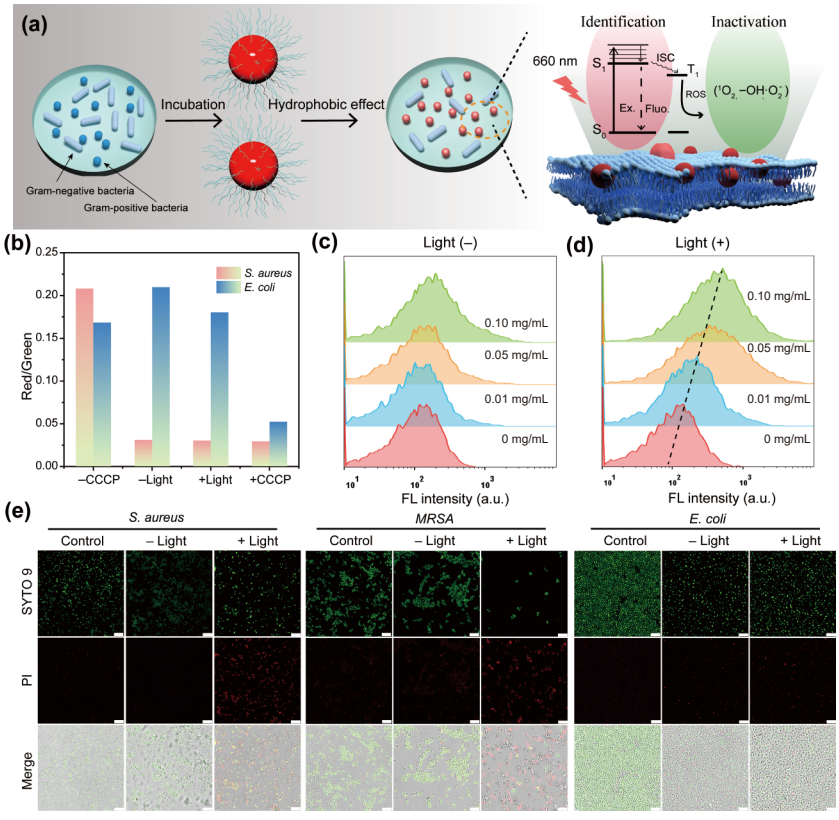

Figure 5 (a) Specific identification of Gram-positive bacteria by the CNDs and the corresponding photodynamic anti-bacteria mechanism. (b) Bacterial membrane potential after CNDs treatment was measure by using a potential sensitive probe. ROS level of mixture of bacteria and the CNDs without 660 nm irradiation (c) and with 660 nm irradiation (d). (e) The CLSM images of bacteria stained by SYTO 9 and PI, respectively. (scale bar = 10 μm).

coefficient value. Subsequently, the CNDs that close contact with the Gram-positive bacteria can be activated instantaneously under the excitation of light. The electrons in singlet excited state after excitation transfer to the triplet excited state through the intersystem crossing, and then the electrons in the triplet state can transfer to surrounding triplet oxygen molecules. In this process, hydroxyl radicals, hydrogen peroxide and singlet oxygen molecules can be produced simultaneously [21]. Then the ROS with strong oxidation ability is directly *in situ* generated on the surface of the bacteria in turn damaging the membrane, leading to the death of bacteria. To investigate the detailed live and death of bacteria, a staining test was performed as follows: The membrane potential of bacteria is due to electrical potential difference between the inside and outside of a living cell membrane, which is necessary for ATP generation during the respiratory process [54]. Dye molecule DiOC2(3) can be used as a probe to detect changes in cell membrane potential, and the decrease of the red/green fluorescence ratio indicates that the cell membrane has been damaged. CCCP is an H^+ ionophore that can alter the permeability of cell membranes, resulting in loss of membrane potential [55]. The +CCCP group was used as a positive control group and –CCCP as a negative control group. Figure S11 in the ESM shows the results of bacterial membrane potential measured by flow cytometry. Under dark conditions, the red/green fluorescent ratio of the mixing system was lower compared to the negative control group (Fig. 5(b)), this is mainly due to the fact that the CNDs can be inserted into the membrane of *S. aureus*, altering membrane permeability leading to a change in bacterial membrane potential. Under 660 nm light irradiation, the red/green fluorescent ratio of the mixing system is close to the positive control group, which was partly due to the insertion of CNDs into the bacterial membrane, changing its membrane potential. Another important reason is that the ROS generated by the CNDs under 660 nm light, and damaged the cell membrane [56]. The scanning electron microscope (SEM) images were taken to observe the membrane change of *S. aureus*. From the SEM images shown in Fig. S12 in the ESM, there was significant damage to the positive bacterial membranes in the light group. After treatment by the CNDs under 660 nm light irradiation, the shape of bacteria changed dramatically, characterization by shrinkage and fusion of cell walls. While for the group of *E. coli* treated with the CNDs and light, the green/red radio is similar to that of the group without treatment. This is consistent with the aforementioned results indicating the CNDs cannot directly attack the cell membrane of the Gram-negative bacteria [57]. To further clarify the mechanism of membrane potential change, the ROS contents of a mixed system of bacteria and the CNDs were measured. The fluorescence intensity of the DCFH-DA is proportionate to the level of intracellular ROS. It can be seen from Fig. 5(c) that the fluorescence intensity of the DCFH-DA in the mixed system does not change with the increase of the CNDs concentration in the absence of light. Under the light irradiation, the groups with higher CNDs concentrations exhibit brighter fluorescence than others (Fig. 5(d)). In general, extracellular ROS only reflect the ROS level produced by bacterial stress reactions. However, extracellular ROS can also penetrate the cell when bacteria died or the membrane was damaged, and the fluorescent signal is thus enhanced, which in turn can also be considered as the reactive oxygen level of the entire system [55].

Live/dead staining assays were performed for different bacteria. SYTO 9 green fluorescent dye is capable of label all bacteria. In contrast, propidium iodide (PI) can across the broken cell membrane and enhanced red fluorescence can be observed after binding to nucleic acids. When the two dyes are mixed in a certain ratio, green fluorescence predominates in normal cells, while cells with damaged cell membranes exhibit a distinct red fluorescence [58]. The CLSM images of SYTO 9 and PI stained bacteria are shown in Fig. 5(e). For the control group and the group without

light, of *S. aureus* and *MRSA*, they show green fluorescence indicating there are no cells died because of cell membrane damage. The group treated the CNDs and light exhibited bright red fluorescence compared with other groups, indicating the severe damage to the bacterial cell membrane. For the *E. coli* group, green fluorescence dominates, indicating that most of the *E. coli* membranes are intact. The toxicity of the CNDs *in vivo* was evaluated by intravenous injection for 1 and 7 days, as shown in Fig. S13 in the ESM. The main organs are then sectioned, there is no symptom of inflammation or lesion in all tissues from histological analysis results. The results solidly demonstrate that the as-prepared CNDs are prominent for selective inactivation of Gram-positive bacteria, implying them promising practice as effective antibacterial agents.

3.5 *In vivo* MRSA-infected therapy

To investigate their therapy application for bacteria-infected wounds, *in vivo MRSA*-infected wounds treatment of mice was evaluated, a detailed process is illustrated in Fig. 6(a). The mice were divided into four groups. *MRSA* infected wounds were treated with PBS (control group), PBS+660 nm light, CNDs and CNDs+660 nm light, respectively. A model of wound was established on mice, although the area of the initial wound was slightly different. Therefore, we used the relative wound area to reflect the rate of wound healing in different treatment groups. Percentage of relative wound area is recorded after treatment each day, as shown in Fig. 6(b). The healing rate of the wounds in the PBS group was lower than that of the CNDs treated group. For the CNDs treated group, the healing rate of CNDs without 660 nm light is superior to PBS group, but low than CNDs+660 nm group, which can be attributed to the daylight environment also promotes the CNDs generate small amounts of ROS increasing the rate of wound healing. Overall, the relative wound area of the CNDs+light group decreases significantly faster in contrast to the other groups. In addition, the number of colony was calculated treated with different conditions, as shown in Fig. S14 in the ESM. The experiment results show that the CNDs also maintain their good antibacterial effect *in vivo* and can effectively reduce the number of bacteria. The bodyweight of the mice in all groups fluctuated within the normal range (Fig. 6(c)). The wound healing process was recorded by the camera shown in Fig. 6(d). On the eighth day, treatment with the CNDs and light significantly inhibited wound infection, resulting in a pronounced decrease in wound size. The corresponding histologic analysis results are shown in Fig. 6(e). In the PBS group, the skin was severely infected with or without 660 nm light, and the boundary between the epidermis and the dermis of the tissue was not clear. The epidermis is severely missing, the dermal matrix is fragmented [59]. On the 8th day after modeling, the masson staining showed the production of a small number of collagen fibers [20]. This may be due to the self-healing ability of the skin [19]. The tissue image after adding CNDs treatment showed that the epidermis and dermis were clearly demarcated. On the whole, 8 days after the administration, the dermal matrix of the CNDs+light treatment group was more abundant, the sebaceous glands and hair follicles were developed, the connective tissues were clearly organized, and the grids were neat and orderly. Masson staining shows larger areas of collagen fibrosis. Elastic fibers are also arranged in a more orderly manner, interwoven into a net and dyed blue-violet [17]. Thus, the photoactivated antibacterial CNDs could efficiently kill bacteria, eliminate the inflammation of the affected area, and further promote wound healing.

4 Conclusions

In summary, CNDs with NIR absorption/emission enabling

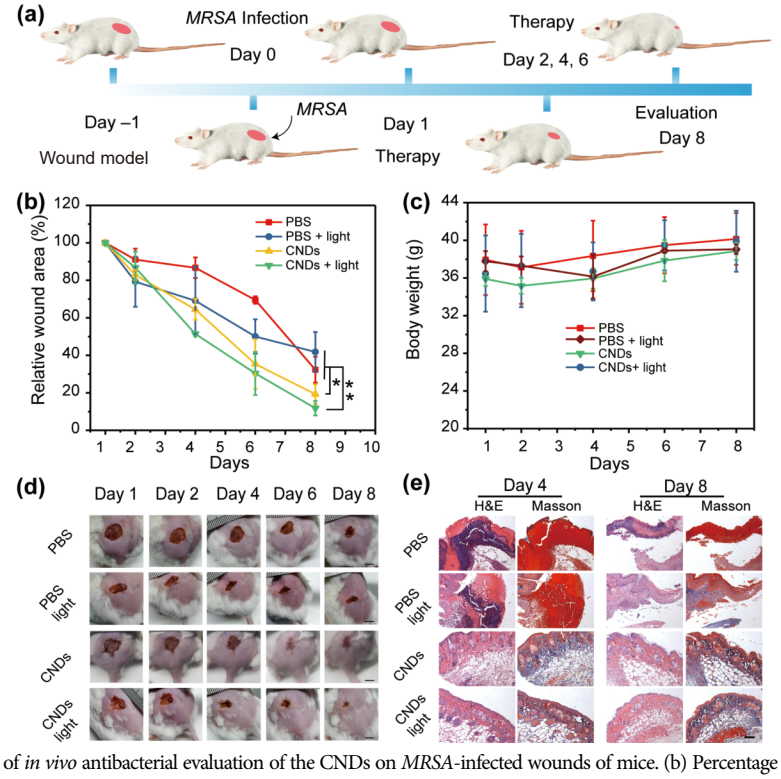

Figure 6 (a) Schematic diagram of *in vivo* antibacterial evaluation of the CNDs on *MRSA*-infected wounds of mice. (b) Percentage of relative wound area of different groups among 8 days (*$p < 0.05$, **$p < 0.01$). (c) Body weight changes within 8 days after different treatments. (d) Photographs of the *MRSA* infected wound treated in different days. The scale for each treatment group is 0.5 cm. (e) The infected wound histologic analyses in day 4 and day 8 with different treatment (PBS, PBS+light, CNDs, CNDs+light). The scale bar in the histologic picture is 100 μm.

effective identification and inactivation of Gram-positive bacteria have been demonstrated. Structural analysis shows that the core of the CNDs consisting of aromatic rings and N heterocycles gives them unique optical properties. The hydrophobic chains on the

surface of the CNDs play a major role in the selective adhesion of Gram-positive bacteria. Thanks to the suitable log *P* value, CNDs can selectively stain Gram-positive bacteria without the need for extra operations to modify the targeting functional groups. The appropriate hydrophobic group of CNDs facilitates its adhesion to the surface of Gram-positive bacteria, and generates ROS *in situ* under 660 nm irradiation. *In vitro* study manifested that CNDs irradiated with 660 nm light for only 5 min can inactivate 99.99% of Gram-positive bacteria. Additionally, the *in vivo* study further demonstrated that CNDs plus light irradiation could efficiently kill *MRSA* to eliminate the inflammation of the affected area, and further promoted wound healing. The ultra-low price, comparable anti-bacteria effect, and reliable safety compared to commercial photosensitizers indicate that CNDs are an excellent new antimicrobial agent. This strategy provides a new idea and insight into the use of CNDs in the field of antimicrobial applications.

Acknowledgements

This work was supported by the National Natural Science Foundation of China (Nos. 11904326, 62075198, U2004168 and 12074348), and China Postdoctoral Science Foundation (Nos. 2019TQ0287 and 2019M662510).

Electronic Supplementary Material: Supplementary material (size distribution of the CNDs, hydrophobic coefficient of the CNDS, TA kinetic process of the CNDs, zeta potential of the CNDs, *S. aureus*, *MRSA* and *E. coli*, the number of *E. faecium* and *Salmonella* treated by the CNDs, membrane potential of *S. aureus* and *E. coli* treated by CNDs, SEM images of *S. aureus* treated with or without the CNDs, hematoxylin and eosin stained slices of bladder, heart, kidney, liver, and lung tissues) is available in the online version of this article at https://doi.org/10.1007/s12274-021-3818-9.

References

[1] Jansen, K. U.; Knirsch, C.; Anderson, A. S. The role of vaccines in preventing bacterial antimicrobial resistance. *Nat. Med.* **2018**, *24*, 10–19.

[2] Saleem, Z.; Saeed, H.; Hassali, M. A.; Godman, B.; Asif, U.; Yousaf, M.; Ahmed, Z.; Riaz, H.; Raza, S. A. Pattern of inappropriate antibiotic use among hospitalized patients in Pakistan: A longitudinal surveillance and implications. *Antimicrob. Resist. Infect. Control* **2019**, *8*, 188.

[3] Kim, D.; Kwon, S. J.; Wu, X.; Sauve, J.; Lee, I.; Nam, J.; Kim, J.; Dordick, J. S. Selective killing of pathogenic bacteria by antimicrobial silver nanoparticle-cell wall binding domain conjugates. *ACS Appl. Mater. Interfaces* **2018**, *10*, 13317–13324.

[4] Yavari, S. A.; Castenmiller, S. M.; Van Strijp, J. A. G.; Croes, M. Combating implant infections: Shifting focus from bacteria to host. *Adv. Mater.* **2020**, *32*, 2002962.

[5] Melander, R. J.; Zurawski, D. V.; Melander, C. Narrow-spectrum antibacterial agents. *Med. Chem. Commun.* **2018**, *9*, 12–21.

[6] Kwon, H. Y.; Liu, X.; Choi, E. G.; Lee, J. Y.; Choi, S. Y.; Kim, J. Y.; Wang, L.; Park, S. J.; Kim, B.; Lee, Y. A. et al. Development of a universal fluorescent probe for Gram-positive bacteria. *Angew. Chem., Int. Ed.* **2019**, *58*, 8426–8431.

[7] Long, S. S.; Miao, L.; Li, R. H.; Deng, F.; Qiao, Q. L.; Liu, X. G.; Yan, A. X.; Xu, Z. C. Rapid identification of bacteria by membrane-responsive aggregation of a pyrene derivative. *ACS Sens.* **2019**, *4*, 281–285.

[8] Deng, Y.; Liu, J. Y.; Li, H. P.; Li, L.; Tu, J. X.; Fang, H. J.; Chen, J.; Qian, F. An improved plate culture procedure for the rapid detection of beer-spoilage lactic acid bacteria. *J. Inst. Brew.* **2014**, *120*, 127–132.

[9] Shang, S. Q.; Chen, G. X.; Wu, Y. D.; Du, L. Z.; Zhao, Z. Y. Rapid diagnosis of bacterial sepsis with PCR amplification and microarray hybridization in 16S rRNA Gene. *Pediatr. Res.* **2005**, *58*, 143–148.

[10] Wang, J. D.; Wang, X. H.; Li, Y.; Yan, S. D.; Zhou, Q. Q.; Gao, B.; Peng, J. C.; Du, J.; Fu, Q. X.; Jia, S. Z. et al. A novel, universal and sensitive lateral-flow based method for the detection of multiple bacterial contamination in platelet concentrations. *Anal. Sci.* **2012**, *28*, 237–241.

[11] Zhang, X. D.; Chen, X. K.; Yang, J. J.; Jia, H. R.; Li, Y. H.; Chen, Z.; Wu, F. G. Quaternized silicon nanoparticles with polarity-sensitive fluorescence for selectively imaging and killing Gram-positive bacteria. *Adv. Funct. Mater.* **2016**, *26*, 5958–5970.

[12] Edgar, R.; Mckinstry, M.; Hwang, J.; Oppenheim, A. B.; Fekete, R. A; Giulian, G.; Merril, C.; Nagashima, K.; Adhya, S. High-sensitivity bacterial detection using biotin-tagged phage and quantum-dot nanocomplexes. *Proc. Natl. Acad. Sci. USA* **2006**, *103*, 4841–4845.

[13] Wang, H. Y.; Hua, X. W.; Jia, H. R.; Li, C. C.; Lin, F. M.; Chen, Z.; Wu, F. G. Universal cell surface imaging for mammalian, fungal, and bacterial cells. *ACS Biomater. Sci. Eng.* **2016**, *2*, 987–997.

[14] Yuan, H. X.; Liu, Z.; Liu, L. B.; Lv, F. T.; Wang, Y. L.; Wang, S. Cationic conjugated polymers for discrimination of microbial pathogens. *Adv. Mater.* **2014**, *26*, 4333–4338.

[15] Jiang, Z. Q.; Vasil, A. I.; Hale, J. D.; Hancock, R. E. W.; Vasil, M. L.; Hodges, R. S. Effects of net charge and the number of positively charged residues on the biological activity of amphipathic α-helical cationic antimicrobial peptides. *Biopolymers* **2008**, *90*, 369–383.

[16] Kang, M. M.; Zhou, C. C.; Wu, S. M.; Yu, B. R.; Zhang, Z. J.; Song, N.; Lee, M. M. S.; Xu, W. H.; Xu, F. J.; Wang, D. et al. Evaluation of structure-function relationships of aggregation-induced emission luminogens for simultaneous dual applications of specific discrimination and efficient photodynamic killing of Gram-positive bacteria. *J. Am. Chem. Soc.* **2019**, *141*, 16781–16789.

[17] Wang, L. W.; Zhang, X.; Yu, X.; Gao, F.; Shen, Z. Y.; Zhang, X. L.; Ge, S. G.; Liu, J.; Gu, Z. J.; Chen, C. Y. An all-organic semiconductor C_3N_4/PDINH heterostructure with advanced antibacterial photocatalytic therapy activity. *Adv. Mater.* **2019**, *31*, 1901965.

[18] Feng, G. X.; Yuan, Y. Y.; Fang, H.; Zhang, R. Y.; Xing, B. G.; Zhang, G. X.; Zhang, D. Q.; Liu, B. A light-up probe with aggregation-induced emission characteristics (AIE) for selective imaging, naked-eye detection and photodynamic killing of Gram-positive bacteria. *Chem. Commun.* **2015**, *51*, 12490–12493.

[19] Liu, W. S.; Ouyang, W. B.; Zhang, C.; Wang, Q. S.; Pan, X. B.; Huang, P. S.; Zhang, C. N.; Li, Y. J.; Kong, D. L.; Wang, W. W. Synthetic polymeric antibacterial hydrogel for methicillin-resistant *Staphylococcus aureus*-infected wound healing: Nanoantimicrobial self-assembly, drug- and cytokine-free strategy. *ACS Nano* **2020**, *14*, 12905–12917.

[20] Tang, J. L.; Chu, B. B.; Wang, J. H.; Song, B.; Su, Y. Y.; Wang, H. Y.; He, Y. Multifunctional nanoagents for ultrasensitive imaging and photoactive killing of Gram-negative and Gram-positive bacteria. *Nat. Commun.* **2019**, *10*, 4057.

[21] Cai, J. Q.; Liu, X. M.; Gao, Z. J.; Li, L. L.; Wang, H. Chlorophylls derivatives: Photophysical properties, assemblies, nanostructures and biomedical applications. *Mater. Today* **2021**, *45*, 77–92.

[22] Knoblauch, R.; Harvey, A.; Ra, E.; Greenberg, K. M.; Lau, J.; Hawkins, E.; Geddes, C. D. Antimicrobial carbon nanodots: Photodynamic inactivation and dark antimicrobial effects on bacteria by brominated carbon nanodots. *Nanoscale* **2021**, *13*, 85–99.

[23] Zhao, X.; Zhao, K. C.; Chen, L. J.; Liu, Y. S.; Liu, J. L.; Yan, X. P. pH reversibly switchable nanocapsule for bacteria-targeting near-infrared fluorescence imaging-guided precision photodynamic sterilization. *ACS Appl. Mater. Interfaces* **2020**, *12*, 45850–45858.

[24] Castano, A. P.; Demidova, T. N.; Hamblin, M. R. Mechanisms in photodynamic therapy: Part one-photosensitizers, photochemistry and cellular localization. *Photodiagn. Photodyn. Ther.* **2004**, *1*, 279–293.

[25] Chen, Y. S.; Zhao, Y.; Yoon, S. J.; Gambhir, S. S.; Emelianov, S. Miniature gold nanorods for photoacoustic molecular imaging in the second near-infrared optical window. *Nat. Nanotechnol.* **2019**, *14*, 465–472.

[26] Kenry; Duan, Y.; Liu, B. Recent advances of optical imaging in the

second near-infrared window. *Adv. Mater.* **2018**, *30*, 1802394.
[27] Li, D.; Han, D.; Qu, S. N.; Liu, L.; Jing, P. T.; Zhou, D.; Ji, W. Y.; Wang, X. Y.; Zhang, T. F.; Shen, D. Z. Supra-(carbon nanodots) with a strong visible to near-infrared absorption band and efficient photothermal conversion. *Light Sci. Appl.* **2016**, *5*, e16120.
[28] Shen, C. L.; Lou, Q.; Liu, K. K.; Dong, L.; Shan, C. X. Chemiluminescent carbon dots: Synthesis, properties, and applications. *Nano Today* **2020**, *35*, 100954.
[29] Liang, Y. C.; Gou, S. S.; Liu, K. K.; Wu, W. J.; Guo, C. Z.; Lu, S. Y.; Zang, J. H.; Wu, X. Y.; Lou, Q.; Dong, L. et al. Ultralong and efficient phosphorescence from silica confined carbon nanodots in aqueous solution. *Nano Today* **2020**, *34*, 100900.
[30] Capilli, G.; Cavalera, S.; Anfossi, L.; Giovannoli, C.; Minella, M.; Baggiani, C.; Minero, C. Amine-rich carbon nitride nanoparticles: Synthesis, covalent functionalization with proteins and application in a fluorescence quenching assay. *Nano Res.* **2019**, *12*, 1862–1870.
[31] Li, H.; Ye, S.; Guo, J. Q.; Wang, H. B.; Yan, W.; Song, J.; Qu, J. L. Biocompatible carbon dots with low-saturation-intensity and high-photobleaching-resistance for STED nanoscopy imaging of the nucleolus and tunneling nanotubes in living cells. *Nano Res.* **2019**, *12*, 3075–3084.
[32] Dong, X. L.; Liang, W. X.; Meziani, M. J.; Sun, Y. P.; Yang, L. J. Carbon dots as potent antimicrobial agents. *Theranostics* **2020**, *10*, 671–686.
[33] Yang, J. J.; Gao, G.; Zhang, X. D.; Ma, Y. H.; Chen, X. K.; Wu, F. G. One-step synthesis of carbon dots with bacterial contact-enhanced fluorescence emission: Fast Gram-type identification and selective Gram-positive bacterial inactivation. *Carbon* **2019**, *146*, 827–839.
[34] Li, H.; Huang, J.; Song, Y. X.; Zhang, M. L.; Wang, H. B.; Lu, F.; Huang, H.; Liu, Y.; Dai, X.; Gu, Z. L. et al. Degradable carbon dots with broad-spectrum antibacterial activity. *ACS Appl. Mater. Interfaces* **2018**, *10*, 26936–26946.
[35] Yang, J. J.; Zhang, X. D.; Ma, Y. H.; Gao, G.; Chen, X. K.; Jia, H. R.; Li, Y. H.; Chen, Z.; Wu, F. G. Carbon dot-based platform for simultaneous bacterial distinguishment and antibacterial applications. *ACS Appl. Mater. Interfaces* **2016**, *8*, 32170–32181.
[36] Qu, D.; Zheng, M.; Li, J.; Xie, Z. G.; Sun, Z. C. Tailoring color emissions from N-doped graphene quantum dots for bioimaging applications. *Light Sci. Appl.* **2015**, *4*, e364.
[37] Peng, J.; Gao, W.; Gupta, B. K.; Liu, Z.; Romero-Aburto, R.; Ge, L. H.; Song, L.; Alemany, L. B.; Zhan, X. B.; Gao, G. H. et al. Graphene quantum dots derived from carbon fibers. *Nano Lett.* **2012**, *12*, 844–849.
[38] Liu, K. K.; Song, S. Y.; Sui, L. Z.; Wu, S. X.; Jing, P. T.; Wang, R. Q.; Li, Q. Y.; Wu, G. R.; Zhang, Z. Z.; Yuan, K. J. et al. Efficient red/near-infrared-emissive carbon nanodots with multiphoton excited upconversion fluorescence. *Adv. Sci.* **2019**, *6*, 1900766.
[39] Bao, X.; Yuan, Y.; Chen, J. Q.; Zhang, B. H.; Li, D.; Zhou, D.; Jing, P. T.; Xu, G. Y.; Wang, Y. L.; Holá, K. et al. *In vivo* theranostics with near-infrared-emitting carbon dots-highly efficient photothermal therapy based on passive targeting after intravenous administration. *Light Sci. Appl.* **2018**, *7*, 91.
[40] Liu, N.; Shi, Y. Y.; Guo, J. R.; Li, H.; Wang, Q.; Song, M. L.; Shi, Z. Y.; He, L.; Su, X. H.; Xie, J. et al. Radioiodinated tyrosine based carbon dots with efficient renal clearance for single photon emission computed tomography of tumor. *Nano Res.* **2019**, *12*, 3037–3043.
[41] Liu, J. J.; Li, D. W.; Zhang, K.; Yang, M. X.; Sun, H. C.; Yang, B. One-step hydrothermal synthesis of nitrogen-doped conjugated carbonized polymer dots with 31% efficient red emission for *in vivo* imaging. *Small* **2018**, *14*, 1703919.
[42] Liu, J. J.; Geng, Y. J.; Li, D. W.; Yao, H.; Huo, Z. P.; Li, Y. F.; Zhang, K.; Zhu, S. J.; Wei, H. T.; Xu, W. Q. et al. Deep red emissive carbonized polymer dots with unprecedented narrow full width at half maximum. *Adv. Mater.* **2020**, *32*, 1906641.
[43] Meng, X.; Chen, T. X.; Li, Y.; Liu, S. Y.; Pan, H.; Ma, Y. N.; Chen, Z. X.; Zhang, Y. P,; Zhu, S. M. Assembly of carbon nanodots in graphene-based composite for flexible electro-thermal heater with ultrahigh efficiency. *Nano Res.* **2019**, *12*, 2498–2508.
[44] Zhang, M. R.; Su, R. G.; Zhong, J.; Fei, L.; Cai, W.; Guan, Q. W.; Li, W. J.; Li, N.; Chen, Y. S.; Cai, L. L. et al. Red/orange dual-emissive carbon dots for pH sensing and cell imaging. *Nano Res.* **2019**, *12*, 815–821.
[45] Liu, S. Q.; Ono, R. J.; Wu, H.; Teo, J. Y.; Liang, Z. C.; Xu, K. J.; Zhang, M. S.; Zhong, G. S.; Tan, J. P. K.; Ng, M. et al. Highly potent antimicrobial polyionenes with rapid killing kinetics, skin biocompatibility and *in vivo* bactericidal activity. *Biomaterials* **2017**, *127*, 36–48.
[46] Jing, P. T.; Han, D.; Li, D.; Zhou, D.; Zhang, L. G.; Zhang, H.; Shen, D. Z.; Qu, S. N. Origin of anisotropic photoluminescence in heteroatom-doped carbon nanodots. *Adv. Opt. Mater.* **2017**, *5*, 1601049.
[47] Wang, L.; Zhu, S. J.; Wang, H. Y.; Wang, Y. F.; Hao, Y. W.; Zhang, J. H.; Chen, Q. D.; Zhang, Y. L.; Han, W.; Yang, B. et al. Unraveling bright molecule-like state and dark intrinsic state in green-fluorescence graphene quantum dots via ultrafast spectroscopy. *Adv. Opt. Mater.* **2013**, *1*, 264–271.
[48] Song, S. Y.; Sui, L. Z.; Liu, K. K.; Cao, Q.; Zhao, W. B.; Liang, Y. C.; Lv, C. F.; Zang, J. H.; Shang, Y.; Lou, Q. et al. Self-exothermic reaction driven large-scale synthesis of phosphorescent carbon nanodots. *Nano Res.* **2021**, *14*, 2231–2240.
[49] Jia, H. R.; Zhu, Y. X.; Chen, Z.; Wu, F. G. Cholesterol-assisted bacterial cell surface engineering for photodynamic inactivation of Gram-positive and Gram-negative bacteria. *ACS Appl. Mater. Interfaces* **2017**, *9*, 15943–15951.
[50] Zhou, C. C.; Xu, W. H.; Zhang, P. B.; Jiang, M. J.; Chen, Y. C.; Kwok, R. T. K.; Lee, M. M. S.; Shan, G. G.; Qi, R. L.; Zhou, X. et al. Engineering sensor arrays using aggregation-induced emission luminogens for pathogen identification. *Adv. Funct. Mater.* **2019**, *29*, 1805986.
[51] Liang, Y. C.; Liu, K. K.; Wu, X. Y.; Lou, Q.; Sui, L. Z.; Dong, L.; Yuan, K. J.; Shan, C. X. Lifetime-engineered carbon nanodots for time division duplexing. *Adv. Sci.* **2021**, *8*, 2003433.
[52] Yan, S. Z.; Chen, S.; Gou, X. B.; Yang, J.; An, J. X.; Jin, X. Y.; Yang, Y. W.; Chen, L.; Gao, H. Biodegradable supramolecular materials based on cationic polyaspartamides and pillar[5]arene for targeting Gram-positive bacteria and mitigating antimicrobial resistance. *Adv. Funct. Mater.* **2019**, *29*, 1904683.
[53] Krishnan, R.; Arumugam, V.; Vasaviah, S. K. The MIC and MBC of silver nanoparticles against *Enterococcus faecalis*—A facultative anaerobe. *J. Nanomed. Nanotechnol.* **2015**, *6*, 285.
[54] Gupta, A.; Mumtaz, S.; Li, C. H.; Hussain, I.; Rotello, V. M. Combatting antibiotic-resistant bacteria using nanomaterials. *Chem. Soc. Rev.* **2019**, *48*, 415–427.
[55] Zhao, W. B.; Du, M. R.; Liu, K. K.; Zhou, R.; Ma, R. N.; Jiao, Z.; Zhao, Q.; Shan, C. X. Hydrophilic ZnO nanoparticles@calcium alginate composite for water purification. *ACS Appl. Mater. Interfaces* **2020**, *12*, 13305–13315.
[56] Zhang, Q.; Ma, R.; Tian, Y.; Su, B.; Wang, K. L.; Yu, S.; Zhang, J.; Fang, J. Sterilization efficiency of a novel electrochemical disinfectant against *Staphylococcus aureus*. *Environ. Sci. Technol.* **2016**, *50*, 3184–3192.
[57] Ucuncu, M.; Mills, B.; Duncan, S.; Staderini, M.; Dhaliwal, K.; Bradley, M. Polymyxin-based photosensitizer for the potent and selective killing of Gram-negative bacteria. *Chem. Commun.* **2020**, *56*, 3757–3760.
[58] Wang, G. M.; Feng, H. Q.; Gao, A.; Hao, Q.; Jin, W. H.; Peng, X.; Li, W.; Wu, G. S.; Chu, P. K. Extracellular electron transfer from aerobic bacteria to Au-loaded TiO_2 semiconductor without light: A new bacteria-killing mechanism other than localized surface Plasmon resonance or microbial fuel cells. *ACS Appl. Mater. Interfaces* **2016**, *8*, 24509–24516.
[59] Lee, M. M. S.; Xu, W. H.; Zheng, L.; Yu, B. R.; Leung, A. C. S.; Kwok, R. T. K.; Lam, J. W. Y.; Xu, F. J.; Wang, D.; Tang, B. Z. Ultrafast discrimination of Gram-positive bacteria and highly efficient photodynamic antibacterial therapy using near-infrared photosensitizer with aggregation-induced emission characteristics. *Biomaterials* **2020**, *230*, 119582.